Spectral filtering of high-order harmonics via optics-free focusing

K. Veyrinas, J. Vábek, C. Valentin, D. Descamps, C. Péjot, F. Burgy, Eric Constant, E. Mével, F. Catoire

Research Article | Vol. 29, No. 19 / 13 Sep 2021 / Optics Express 29813

Optics EXPRESS

Spectral filtering of high-order harmonics *via* optics-free focusing

K. VEYRINAS,[1] J. VÁBEK,[1,2,3] C. VALENTIN,[1] D. DESCAMPS,[1] C. PÉJOT,[1] F. BURGY,[1] E. CONSTANT,[4,5] E. MÉVEL,[1] AND F. CATOIRE[1,6]

[1]*Centre Lasers Intenses et Applications, Université de Bordeaux-CNRS-CEA, 33405 Talence Cedex, France*
[2]*ELI Beamlines Centre, Institute of Physics, Czech Academy of Sciences, Za Radnicí 835, 25241 Dolní Břežany, Czech Republic*
[3]*Czech Technical University in Prague – Faculty of Nuclear Sciences and Physical Engineering, Jugoslávských partyzánů 1580/3, 160 00 Praha 6, Czech Republic*
[4]*Université de Lyon, Université Claude Bernard Lyon 1, CNRS, Institut Lumiére Matiére (ILM), 69622 Villeurbanne, France*
[5]*eric.constant@univ-lyon1.fr*
[6]*fabrice.catoire@u-bordeaux.fr*

Abstract: Controlling the wavefront of an extreme ultraviolet (XUV) high-order harmonic beam during the generation process offers the capability of modifying the beam properties without resorting to any XUV optics. By characterizing the XUV intensity profile and wavefront, we quantitatively retrieve both the size and the position of the waist of each harmonic generated in an argon jet. We show that optics-free focusing can occur under specific generating conditions leading to XUV focii of micrometer size. We also demonstrate that each focus is located at distinct longitudinal positions. Using this remarkable XUV wavefront control combined with near focus spatial selection, we experimentally demonstrate efficient and adjustable spectral filtering of the XUV beam, along with a strong rejection of the fundamental beam, without using any XUV optics. The experimental results are compared with simulations providing the impact of the filtering on the temporal profile of the XUV field. It shows that the attosecond structure is preserved and that the beam is more homogeneous after the filtering, thereby reducing the longitudinal focii shift. This is a major step to achieve high XUV intensity and probing ultrafast processes with an improved resolution.

1. Introduction

High-order harmonic generation (HHG) [1,2] is a highly non-linear process producing coherent light in the extreme ultraviolet (XUV) domain and is nowadays commonly used as a table-top source of femtosecond and attosecond pulses [3–5]. Numerous applications rely on these HHG-based sources such as ultrafast molecular dynamics [6–8], coherent diffraction imaging [9,10], non-linear optics in the XUV spectral range [11,12], for instance. A major remaining challenge consists in controlling the spatial and temporal properties of the XUV beam in order to ensure homogeneous characteristics of the XUV radiation as several studies observed strong spatio-temporal couplings in the XUV beams [13,14]. Controlling the spatio-temporal properties is also crucial from the practical point of view. For instance, the increase of the XUV intensity, which allows for performing experiments involving non-linear processes, can be done by either increasing the energy, shortening the pulse duration of the XUV pulse or by properly focusing the XUV beam [15]. Nevertheless, the focusing properties strongly depends on the harmonic order [13,15–18] so that the control of the XUV beam properties continues to be oppugned. Moreover, focusing the XUV beam can induce significant distortion of the pulse temporal profile when the harmonics have different spatial characteristics [13,19].

#436086 https://doi.org/10.1364/OE.436086
Journal © 2021 Received 21 Jul 2021; revised 19 Aug 2021; accepted 20 Aug 2021; published 31 Aug 2021

Optics EXPRESS

Focusing properties have been controlled by techniques based on reflective mirrors for example metallic toroidal mirror [20] or Mo/Si parabolic mirror [21]. Unfortunately, these techniques can induce optical aberrations leading to pulse broadening and low reflectivity [19,22] for broadband XUV pulses.

Recently, Quintard *et al.* [23] have demonstrated the possibility of generating harmonics as either diverging or converging beams showing the ability to control the XUV beam spatial properties directly via the generation process. This coherent properties comes along with other possibilities such as refractive optics [24] or opto-optical modculation [25]. The dependence of the focusing properties with harmonic order and quantum path were also reported with other setups in [15,17,26]. The so-called optics-free focusing demonstrated by Quintard *et al.* is the result of XUV front-phase coherent control during the generation process. This coherent process also provides a control of the XUV beam divergence. We use this property to achieve highly efficient spectral filtering of HHG over a controllable bandwidth which also provides homogeneous characteristics of the filtered XUV beams.

The paper is organized as follows: First the SWORD technique [27] for spectrally-resolved intensity profile and wavefront characterization of the XUV radiation is presented. This technique allows to retrieve the waist of each generated harmonic for different positions of the gas jet versus the laser focus position. It constitutes a direct measurement of optics-free focusing and we show that (*i*) real focii as small as 5 μm are achieved after the gas jet by controlling the XUV beam without resorting any XUV optics and (*ii*) the harmonics are usually not focused all at the same longitudinal position even when they are issued from the short path emission and that the focii can be larger than the XUV confocal parameter. These experimental observations imply that the XUV bandwith and the attosecond temporal characteristics evolve with the propagation and are therefore space-dependent. We use a pinhole to spatially filter the XUV beam near focus and show that this selection results in spectral selection of harmonics. Then we present the theoretical model that is used to compare with experiments. This model is employed for retrieving the focusing properties of the XUV beam and also to determine the far-field properties of the beam, in particular the impact on the spectral selection.

2. Experimental setup and results

2.1. Experimental setup

Experiments have been performed on the terawatt Ti:sapphire Eclipse laser facility at CELIA delivering 800-nm, 40-fs pulses at a 10-Hz repetition rate. The experimental setup is described in detail in [23]. Briefly, we use a laser beam that was spatially filtered to ensure a near-Gaussian spatial profile (M^2_{vert} = 1.02 and M^2_{hor} = 1.09) delivering a usable 4.5 mJ pulse energy in the generation chamber. Pulses are then compressed under vacuum down to 40 fs and propagate under vacuum after the compressor. Correction of the IR wavefront is performed under vacuum by reflecting the beam on a deformable mirror (HIPAO, ISP System) coupled to an HASO wavefront sensor (Imagine Optic) for optimization, allowing for Strehl ratio higher than 0.97. IR pulses are then focused by a 2-m focal length spherical mirror (the typical achieved peak intensity is 5×10^{14} W/cm^2 at focus with an iris diameter of 20 mm) onto a pulsed neon jet mounted on a translation stage able to move over 15 cm along the laser focus. At focus, the IR beam has a waist of 85 μm and the confocal parameter is $b = 2z_r = 5.6$ cm. Negative (resp. positive) values of z_{jet} means that HHG occurs upstream (resp. downstream) of the IR focus. The generated harmonics are then transmitted through the 500-μm-thick entrance slit of a flat-field XUV spectrometer before being dispersed by a grazing incidence Hitachi spherical grating (1200 gr/mm) onto an XUV detector consisting of a 40-mm-diameter dual micro-channel plates (MCPs) and a phosphor screen imaged by a CCD camera. The MCP is located 2.9 m after the laser focus. A movable pinhole with 140 μm diameter, drilled in an unpolished dielectric plate, can be inserted 37 cm after the IR focal plane either to characterize the XUV intensity spatial profile and wavefront or

Optics EXPRESS

to spectrally filter the harmonic beam. At this position, the pinhole can withstand the IR fluence without damage.

2.2. Spatial characteristics measurements of the XUV beam

Characterization of the XUV wavefront has been performed using the SWORD (Spectral Wavefront Optical Reconstruction by Diffraction) technique [27]. This technique is not the only one allowing for the retrieve of the harmonic wavefront see [28] for example, but the SWORD technique is probably the most direct one. It consists of recording the diffraction pattern of the XUV radiation transmitted through a slit – a pinhole in our case – while scanning the slit across the XUV beam. For each harmonic, the spatial phase of the sampled wavefront slice is extracted from the relative vertical position of the diffraction pattern's centroid with respect to the pinhole position. The corresponding local XUV yield is obtained by integrating the signal of the diffraction pattern on the MCP.

In Fig. 1 are presented the results of the SWORD measurement for harmonics H31,H45 and H49. Fitting the measured XUV intensity profile (a) and reconstructed spatial phase (b) by Gaussian and quadratic functions, respectively, provides the beam size w_q and the radius of curvature R_q of each harmonic wavefront in the pinhole plane. We measure a near Gaussian spatial intensity profile and observed that the beam size and wavefront curvature change with the harmonic order and gas jet position. For $z_{jet} = -35$ mm, we obtain $w_q = 309$, 240, and 174 μm and $R_q = 363$, 396, and 382 mm for harmonics H31, H39 and H47, respectively in the plane of the pinhole. From the SWORD measurements, we can infer that the XUV beam has both the front phase and intensity profile of a Gaussian beam and we can therefore consider that each harmonic propagates like a Gaussian beam (see the fit of the intensity distribution and front phase in Fig. 1).

(a) Intensity profile (b) Phase profile

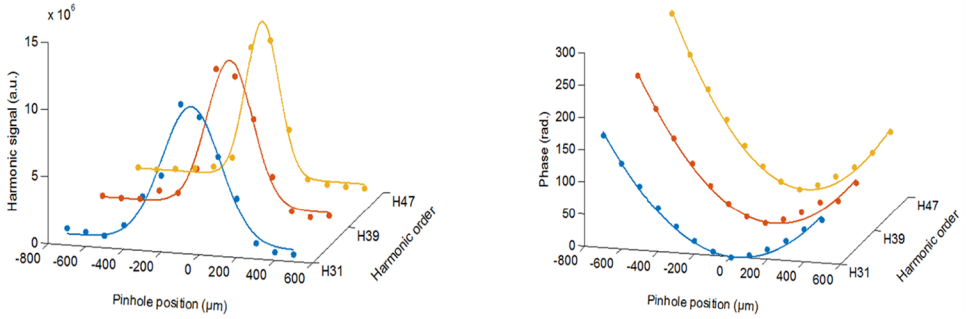

Fig. 1. (a) Measured intensity profile (dots), Gaussian fit (line) and (b) reconstructed spatial phase of the wavefront (dots), quadratic fit (line). The plots are shown for harmonics H31 (blue), H39 (red) and H47 (orange), using the SWORD technique for $z_{jet} = -35$ mm.

Consequently, from the intensity profile and wavefront characterization we can retrieve both the size $w_{q,0}$ and the position $z_{q,0}$, with respect to the gas jet position, of the waist of each harmonic beam:

$$w_{q,0} = \frac{w_q}{\sqrt{1 + \left(\frac{\pi w_q^2}{\lambda_q R_q}\right)^2}} \tag{1}$$

$$z_{q,0} = \frac{R_q}{1 + \left(\frac{\lambda_q R_q}{\pi w_q^2}\right)^2}. \tag{2}$$

Optics EXPRESS

In Fig. 2, we present the results of this analysis for harmonics H31, H35, H45 and H49, as a function of the gas jet position z_{jet} relative to the IR focus. Strong dependencies of $w_{q,0}$ (Fig. 2(a)) and $z_{q,0}$ (Fig. 2(b)) with harmonic order q and z_{jet} are observed. In particular, we emphasize the longitudinal separation of the harmonic waists of the different harmonics and we observed that this separation is comparable or larger than the XUV confocal parameter. Depending on the gas jet position, the waist size varies from ≈ 5 μm to ≈ 15 μm for H31-H35 and from ≈ 4 μm to ≈ 20 μm for H45-H49. As the harmonic order increases, the maximum waist size is larger and obtained for generation further upstream of the IR focus that corresponds to a position where the XUV focus is located after the gas jet. On the contrary, the minimum waist size decreases when the harmonic order increases and it is obtained when the jet is in the range of 0 to -10 mm, *i.e.* in a position range where the XUV focus is before the gas jet. In Fig. 2(b), the gas jet position is denoted by the dashed line. Below (resp. above) this line, the XUV waists are located before (resp. after) the generating medium and thus are virtual (resp. real). For $z_{jet}>0$ mm, the waists of harmonics are virtual and the XUV radiations are emitted as diverging beams. For $z_{jet}<-15$ mm, the waists are real meaning that harmonics are emitted as converging beams. We observe that these converging XUV beams are focused to spot size of $5-20$ μm at distances up to 120 mm (*i.e.* $4.3 \times z_{R-IR}$) after the IR focus. Overall, these measurements are in good qualitative agreement with the results reported by Quintard *et al.* [23] where harmonic optics-free focusing was introduced and observed experimentally with the inversion of the spatial chirp of the XUV beam throughout their free propagation. Our results, showing the evolution of $w_{q,0}$ and $z_{q,0}$ for each harmonic, constitute the first quantitative measurement of XUV optics-free focusing obtained by HHG. Moreover we show a real focusing distance of up to 4 times the Rayleigh parameter of the IR pulse and XUV focii sizes down to a few microns. Unfortunately, from our results we show that these two properties, small focus size and long focus position, cannot be reached concomitantly. We show in this work how by modifying the phase profile of the IR beam we are able to control the wavefront of the XUV beam. The IR phase profile is not performed actively by using the deformable mirror but by moving the gas jet position. This is strictly equivalent as applying a specific spatial quadratic phase to the deformable mirror and can be compared to our results. More complex phase profile can be generated and used and will be done in a forthcoming work. The optics-free focusing presented in this work can lead to high XUV intensities. By considering a 10 mJ IR pulse and an HHG efficiency of 10^{-5}, we get 100-nJ energy per harmonic. Assuming a 5-fs pulse duration it leads to an intensity of 10^{13} W/cm^2 for a

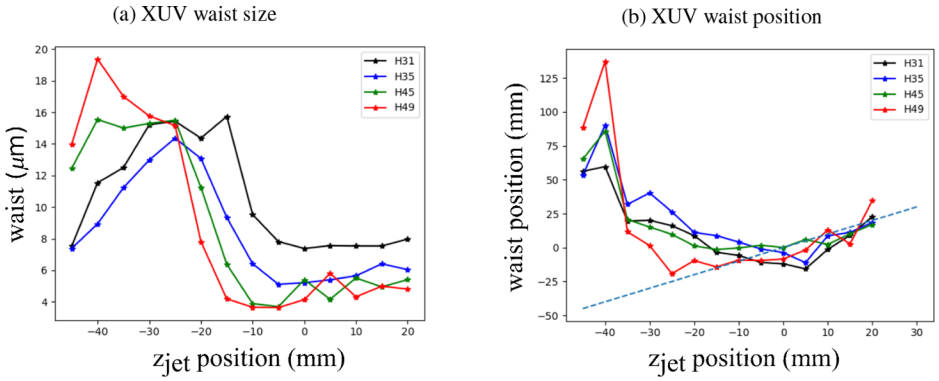

Fig. 2. (a) Size $w_{q,0}$ and (b) position $z_{q,0}$ of the waist of harmonics H31 (black), H35 (blue), H45 (green) and H49 (red) as a function of the gas jet position. In (b), the XUV waists located below (resp. above) the blue dashed line, *i.e.* that is located before (resp. after) the generating medium, corresponds to virtual (resp. real) source.

Optics EXPRESS

single harmonic. Higher intensities could be obtained by optics-free focusing when all harmonics are focused at the same position. This should be possible by controlling the IR intensity profile and wavefront for example by using flat-top spatial profile of the driving beam since in this case the spatial dependence of intensity with radius is identical for all harmonics namely flat.

2.3. Spectral control by spatial filtering

Spatially-separated focii can be useful for spectral selection of high-order harmonics in dispersion free configuration. Here, we use the control of the XUV beam properties and propagation through a 140 μm-diameter pinhole located few z_R after the XUV focii in order to perform XUV spectral filtering. This spectral selection is thus performed without using XUV optics.

The filter transmission is measured by comparing the spatially-resolved HHG spectrum transmitted through the pinhole centered on the pathway of the harmonics with the reference obtained without the pinhole, as shown in Fig. 3(a) and (b) for $z_{jet} = -58$ mm. The transmission factor, or transmittance (T) is defined as the ratio of the HHG spectra integrated over the spatial coordinate with and without pinhole (Fig. 3(c)). Fig. 3(d) displays the measured transmission

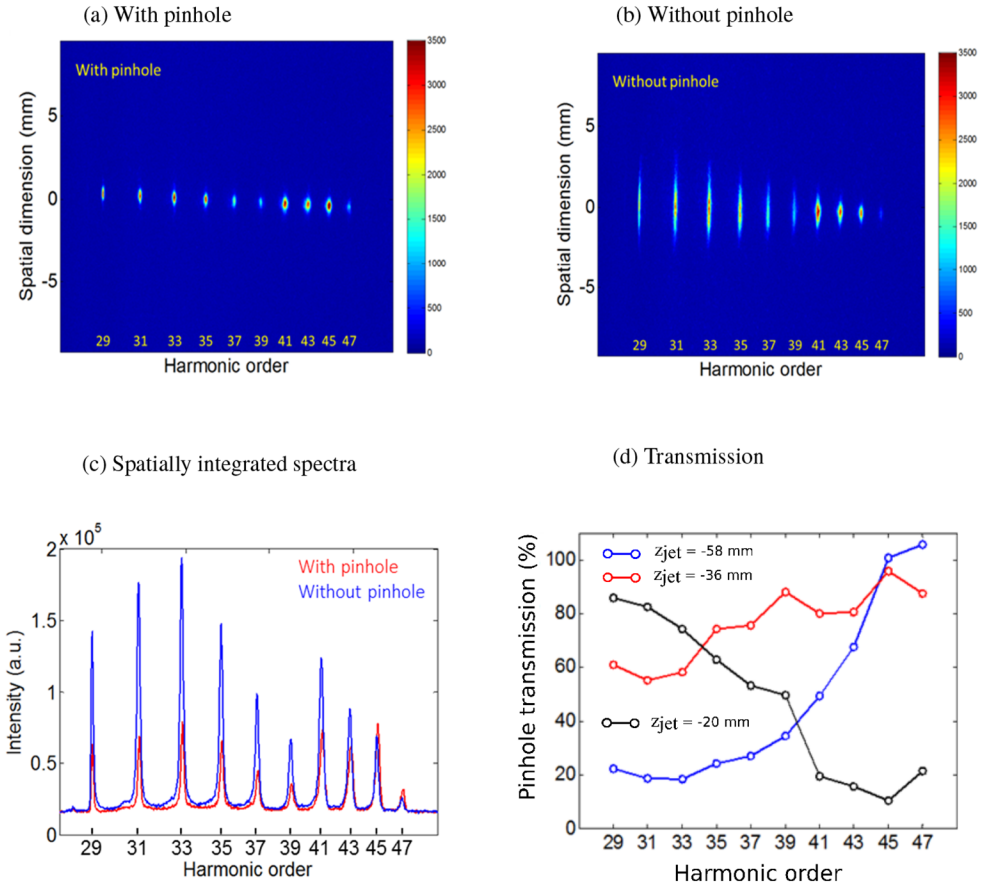

Fig. 3. Far-field spatially-resolved HHG spectrum measured for z_{jet} = -58 mm with (a) and without (b) the pinhole centered on the XUV path.(c) Corresponding HHG spectra after summing over the spatial coordinate. (d) Measured transmission of harmonics H29 to H47 for z_{jet} = -58 (blue), -36 (red) and -20 mm (black). The error bar of the transmittance (not shown here) is estimated to be within 10 %.

Optics EXPRESS

factors of harmonics H29 to H47 for z_{jet} = -58, -36, -20 mm and clearly shows that the characteristics of this filter are fully tunable by adjusting the gas jet position with respect to the IR focus. For $z_{jet} = -20$ mm (black curve), we observe a high transmission (>80 %) of harmonics H29-H31 and an attenuation (T < 20 %) of harmonics H41-H47. It corresponds to a low-pass XUV filter. For $z_{jet} = -58$ mm (blue curve), the situation is reversed with very high (close to 100 %) and low (T ≈ 25 %) transmissions of harmonics H45-H47 and H29-H37, respectively. This is a high-pass XUV filter. In both cases, the spectral selectivity and contrast ensure a proper selection of a group of harmonics. On the other hand, for $z_{jet} = -36$ mm (red curve), band-pass transmission is also achieved with 60 < T < 90 % over the H29-H47 range, allowing for producing broadband XUV pulses. When refocused into an experiment, this can lead to intense attosecond pulses. The three configurations: high-pass, low-pass and broadband can be selected simply by moving the jet position. In all these cases, we observed that the harmonic beam transmitted through the pinhole had all very similar spatial profiles in the far field while they are very different without the pinhole. The IR beam is also poorly transmitted by the pinhole that is much smaller than the IR beam size. Therefore, the XUV filtering is accompanied by a strong attenuation of the IR beam after the pinhole. We estimate, using simple transmission law of a Gaussian beam going trough an aperture, the transmission to be less than 1 % in our conditions.

Furthermore, the transmitted IR beam will be strongly divergent after the pinhole because of diffraction [29] and therefore poorly intercepted by any optics that could be located downstream in an experiment. Here, we point out that the present approach does not require the use of any XUV optics and thus does not suffer from limitations inherent to this energy range as encountered with traditional optical techniques.

3. Theoretical model

In this section, the theoretical model used hereafter is presented. The basic physical picture of harmonic propagation is inferred from a model of an XUV beam generated in a thin target that has been presented and detailed in [30] and [23]. Assuming the generation in a thin medium [31] and that the IR beam is not affected by propagation in the generating medium, the longitudinal effect, also called phase-matching, can be treated separately since it appears as a prefactor [30]. The spatial distribution of the XUV beam is obtained at a distance D by a Fraunhoffer-like diffraction pattern as follows:

$$E(z_{jet}; z, \rho, \omega) = \int_0^\infty \tilde{\rho} d\tilde{\rho} \quad \frac{e^{-i\frac{k(\omega)\tilde{\rho}^2}{2D}}}{D} J_0\left(\frac{k(\omega)}{D}\tilde{\rho}\rho\right) d(z_{jet}; \tilde{\rho}, \omega). \tag{3}$$

J_0 is the zeroth order Bessel function and d is the Fourier transform from time to frequency of the dipole generated in the medium. Note that the extra phase $e^{-i\frac{k(\omega)\tilde{\rho}^2}{2D}}$ is often neglected in models but it is necessary to be considered in order to describe the situation at intermediate distances, and in particular the focusing properties of the XUV beam, and not only the far-field. It is easy to show that the propagator defined in Eq. (3) is exact for the Gaussian modes. If this extra phase term is removed, the regular Fraunhoffer is recovered, and the diffraction pattern is homothetic with D, thereby preventing the observation of optics-free focusing. We used two methods for calculating the dipole d. One model relies on the resolution of the Time-Dependent Schrodinger Equation (TDSE) and the other one on the dipole model [30]. The TDSE is solved for computing the atomic dipole in a 1D geometry and using the single active electron approximation and will be called the TDSE-model hereafter. The dipole model expresses the dipole as: $d = I^{q_{eff}/2} e^{i\varphi_q(r)}$ with

$$\varphi_q(r) = q\varphi_{IR}(r) - \alpha_q I_{IR}(r). \tag{4}$$

Optics EXPRESS

I is the space dependent intensity of the IR pulse. q_{eff} and α_q are two coefficients that are calculated using the saddle point approximation in the frame of the Strong Field Approximation model [32]. The phase term is composed to two contributions. When only the first term is considered, the XUV and IR wave fronts are commensurate. The second contribution, proportional to the IR intensity I_{IR}, is the atomic phase intrinsic to the HHG process. The α_q coefficient depends on harmonic order q and the class of trajectories (short or long) [33,34]. Both spatial phase terms can be of comparable amplitude for the short path emission and the spatial evolution of $\varphi_q(r)$ changes the curvature of the XUV wavefront with z_{jet}. We also assume that result of the integration over $\tilde{\rho}$ is essentially determined by the value close to $\tilde{\rho} \approx 0$ so that the intensity dependence of the atomic phase αI reduces to its quadratic dependence in r. Consequently, the total phase is quadratic in r, with an effective radius of curvature R. R is built up of two radii of curvature R_{IR} and R_{atom} which are respectively associated with the generating beam and the intrinsic HHG spatial phase. These radii of curvature are linked by the relation $\frac{1}{R} = \frac{1}{R_{IR}} + \frac{1}{R_{atom}}$. Both terms ($R_{IR}$ and R_{atom}) can have similar amplitudes. While R_{atom} is always positive, R_{IR} can either be negative (when the IR beam is converging, *i.e.* the gas jet is placed before the IR focus) or positive (when the IR beam is diverging, *i.e.* the gas jet is placed after the IR focus). It is thus possible to control the curvature of the XUV wavefront by changing the interaction parameters such as the IR intensity, the value of α_q and the gas jet position with respect to the IR focus (z_{jet}) that defines the IR wavefront radius of curvature. Using this model, the propagation can be performed analytically and is called the Gaussian-model in the following since the spatial distribution of the XUV beam remains Gaussian (see [17,23,35,36] for more detail and other various configurations).

4. Comparison between experimental and theoretical results and discussions

4.1. Transmission and spectral selection

In our simulations we set the IR beam waist at 85 μm (z_R = 28.4 mm), the intensity at focus to 4×10^{14} W/cm^2. The pulse duration was set to 40 fs FWHM for TDSE calculations and the dipole model. From each model, we can determine the size of the HHG beams on the pinhole and then calculate the spectral XUV transmission through it as realized experimentally. The results for the Gaussian-model and the TDSE-model are presented in Fig. 4 in the upper and bottom part respectively.

The left panels are the plot of the pinhole transmission as a function of z_{jet} for harmonics $H29 - H37 - H47$ and the right panels are the plot of the transmission as a function of harmonic order for $z_{jet} = -5, -10, -15 - 20, -25$ mm. The Fig. 4(b) and Fig. 4(d) show similar trends. For large negative values of z_{jet}, the transmittance shows an increase with harmonic order. On the other hand, for small values of z_{jet}, the transmittance decreases with harmonic order. For intermediate values of z_{jet}, the transmittance shows a bell like shape ranging from 20 % to 100 %. This can be compared with experimental results showing an overall agreement that corresponds to the mentioned low-pass, high-pass and band-pass filter. Despite the overall agreement of the trend, transmittances computed for both models as a function of z_{jet} for a given harmonic are different. Transmittance distribution presents one maximum for Gaussian-model, and two maxima are observed for TDSE-model. In the TDSE-model, the double hump structure is due to the evolution of α_q with intensity. In the Gaussian-model α_q is kept constant. For short trajectories, as considered here, the value of α_q is small when the harmonic belongs to the plateau (high intensity) and larger when the harmonic is in the cut-off (low intensity). We observe primary maxima located at -7 mm, -15 mm, -25 mm for H29, H37 and H47 respectively. These maxima, obtained from Fig. 4(c), are in accordance with Fig. 4(a). The secondary maxima are located at -40 mm, -30 mm, -20 mm for H29, H37 and H47 respectively. In the latter case, the secondary peak is mixed with the primary one leading to a broad peak. The second peak is due to the sudden change of α when the peak intensity decreases with z_{jet} and when the harmonic enters the

Optics EXPRESS

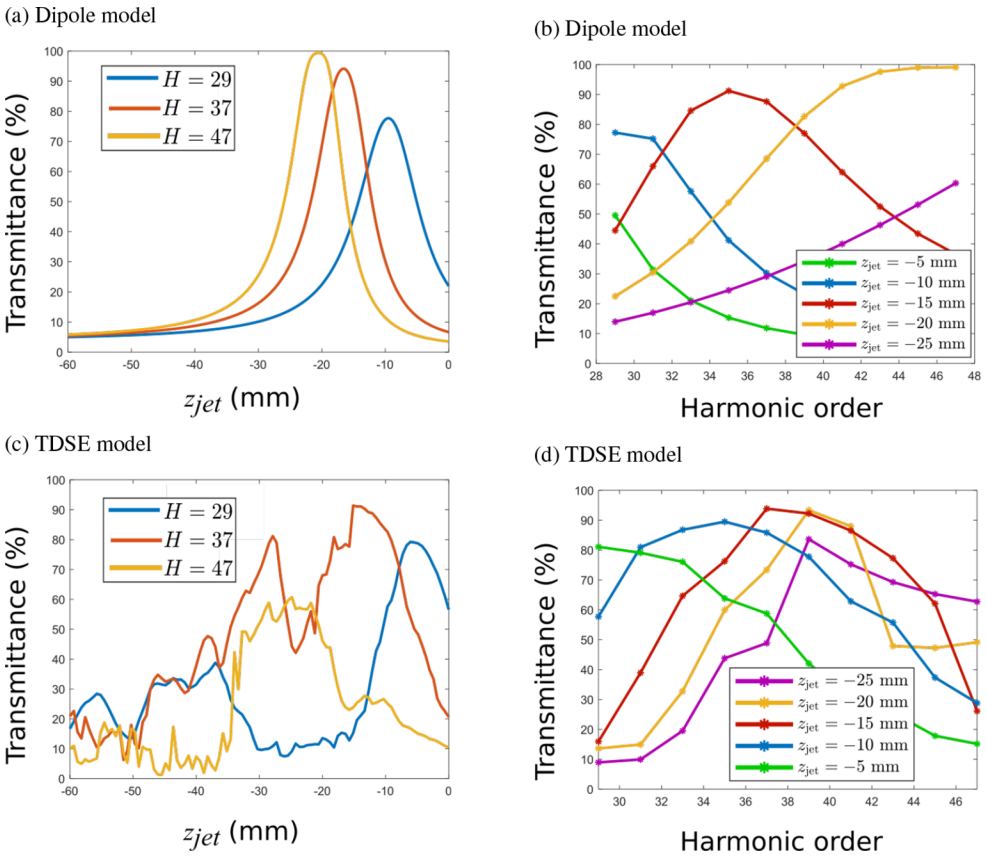

Fig. 4. (a) Transmittance map as a function of gas jet positions for H29, H37 and H47 computed with the dipole model and Gaussian propagation presented in Sec. 3. (b) Transmittance versus harmonic order for 5 gas jet positions. The corresponding results obtained with TDSE model are given in (c,d)

cutoff [34]. It is also expected that when the harmonic order increases, the values of α will span a smaller range of value near cut-off resulting in a closer or even merging peaks as described before. The expression of the harmonic cut-off is $q_c = \frac{3.2I}{4\omega_{IR}^3} + \frac{Ip}{\omega_{IR}} = q_c^0 + \frac{Ip}{\omega_{IR}}$ with I, ω_{IR}, I_p expressed in a.u. If we assume a Gaussian intensity profile, we can estimate at which value of z the peak intensity of a given harmonic toggles in the cut-off. This value is $z_{cut} = z_{R-IR}\sqrt{\left(-1 + \frac{3.2I_0}{4q_c^0\omega_{IR}^3}\right)}$ with I_0 being the peak intensity at focus expressed in a.u. Applying the latter formula we obtain the position of the secondary maximum located at -43 mm, -31 mm, -21 mm for harmonics H29, H37 and H47 respectively. These values are in good agreement with what is observed from the TDSE numerical simulation. The experimental distribution of the transmittance as a function of the jet position is presented in Fig. 5 for harmonics $H29$, $H37$ and $H41$.

From this plot we observed a similar trend as compared to Fig. 4(c).

In particular for harmonic 29, the maximum is observed close to $z_{jet} \approx -10$ mm with an experimental peak that appears broader compared to our simulations. A secondary peak at -25 mm can eventually be guessed, but it is not positioned as far away from the IR focus point as compared to the theoretical value. For harmonic $H37$ two peaks are observed at -15 mm and -25 mm. These values are in accordance with the TDSE results. Last, for harmonic $H41$ a

Optics EXPRESS

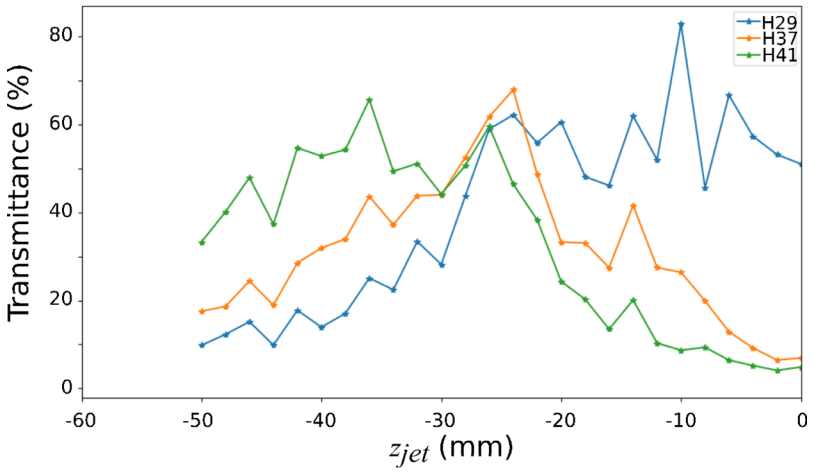

Fig. 5. Experimental transmittance for harmonics $H29$, $H37$ and $H41$ as a function of z_{jet}.

broad peak is observed around −25 mm, which is in accordance with what could be extrapolated with the theoretical data which present a broad peak located at −25 mm. Experimentally it is hard to fairly attribute peak position and compare with theoretical simulations but the overall comparison of experimental and theoretical spectra shows similar trends. This can be due to the sensitivity of the transmittance distribution as a function of z_{cut} with intensity, and to the intensity fluctuation of the laser that can blur the signal. Nevertheless, the laser stability is good enough to retrieve the general trend even if the fine detail predicted by the TDSE calculations cannot be reproduced quantitatively. From a practical point of view, the method is robust enough to adjust the transmittance of a given harmonic as can be seen in Fig. 5 and Fig. 4(d).

In this section, we have shown that the transmittance of the XUV beam through the pinhole can be controlled by changing z_{jet}. Far from the IR focus, we obtained a high pass filter with T above 90 % for highest harmonic order. Near the IR focus, we obtain a low-pass filter with T reaching 80 % for the lowest order. In between, pass-band filter can be obtained for intermediate gas jet position (around −10 mm) which preserves a high transmission. We also observed that the beams had a similar spatial profile after transmission through the pinhole as observed experimentally. In the following, we investigate the effect of the XUV beam spatial filtering on the temporal profile in the far-field.

4.2. Spatio-spectral profiles of the XUV field

Fig. 6(a) presents the plot of the on-axis spectrum in the near-field (black curve) and in the far-field for a fixed $z_{jet} = -15$ mm position where the curve of transmission through the pinhole is the most flat as a function of harmonic order which corresponds to the band-pass configuration. This configuration is chosen since it is the case where the attosecond pulse train is the most sensitive to the frequency bandwidth.

The red curve of Fig. 6(a) is the spectral distribution obtained on-axis after free propagation while the blue curve is the distribution of the on-axis spectrum after propagation through the pinhole. Clearly the spectra remain almost unchanged (on the log. scale) if the pinhole is used or not. This is due to the fact that we selected the position of the gas jet where the transmission is almost flat and only the on-axis field is observed. The spectra show well pronounced odd harmonics. This is the signature of the short trajectories selection in the far-field. In the case of the near-field (e.g. in the emission plan, the black curve of the figure) the spectrum is more heckled.

Optics EXPRESS

(a) Harmonic spectra (b) Temporal profile

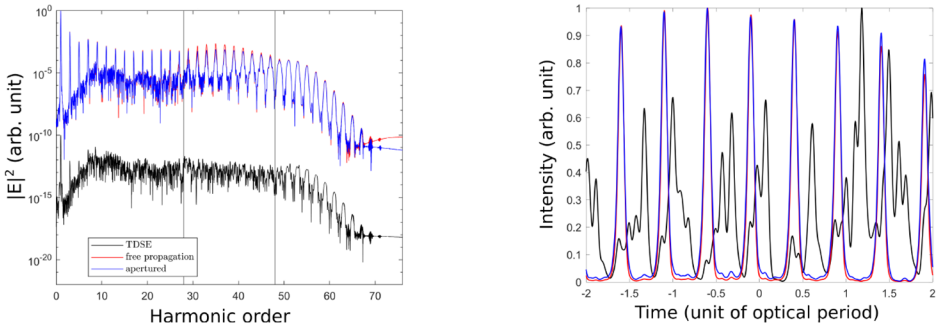

Fig. 6. (a) The spectra for the source term (black curve), and the macroscopic spectrum calculated on-axis with (blue curve) and without pinhole (red curve) computed with TDSE-model at $z_{jet} = -15$ mm. (b) The XUV intensities within few cycles of the fundamental field for the source term (black curve) and propagated fields (red: free propagation; blue: apertured)

We now concentrate on the temporal profile. To do so, we Fourier-transform back the spectra selected in the range H29 to H47 as indicated by the vertical lines in Fig. 6(a). The results are plot in Fig. 6(b). The black curve is the near-field on-axis temporal profile, while the red and blue curves are the far-field on-axis temporal profile for the free propagation and the propagation through the pinhole respectively. The black curve shows an irregular temporal profile. The contribution stemming from the interference of the short and long trajectories leads to a complex field. On the contrary, in the far-field on-axis case, where only the short trajectories contribute, we observe a more regular temporal evolution [37]. Moreover, only a slight change of the temporal profile is obtained when applying or not the spatial filtering. Similar behavior have been observed for other gas jet positions ($z_{jet} = -25$ mm and -5 mm results not shown) having a different transmittance function. This is the consequence of the well known long-trajectories filtering (due to large divergence) but what is interesting here is that it has been obtained in the thin medium approximation, i.e. without including phase-matching. The filtering observed in this configuration is only due to free-propagation after the pinhole in one case and after generation in the other. By measuring few FWHM in the train, we estimate that we can reach pulse duration down to 200 as for $z_{jet} = -15$ mm for these specific generation conditions.

For experiments based on refocusing in order to increase the XUV intensity, the global evolution of the temporal profile is crucial if one also wants to produce short pulses. For getting the most reliable field at focus, where all the field (not only $\rho \approx 0$) can contribute to the attosecond profile, the study of the evolution of the off-axis spatio-temporal field is primordial. This is the purpose of the next section. We will restrain our study to the far field observable since this is the only one that can be compared with experiments.

In Fig. 7 the spatially resolved spectra when the gas jet is positioned -15 mm before the IR focus without (a) and with (b) filtering are presented.

The first observation is the effective reduction of harmonic beam size in the apertured case where the size presents much less variation from one harmonic to the other. In order to get a quantitative evolution of the radial distribution of energy we plot the integration of this 2D distribution over the harmonic order. It leads to the energy distribution as a function of ρ (spatial profile) as shown in Fig. 8.

Clearly the aperture considerably reduces the spatial extension of the XUV beam in the far field. From this distribution, we define the critical radius ρ_c, for which half of the energy is

Optics EXPRESS

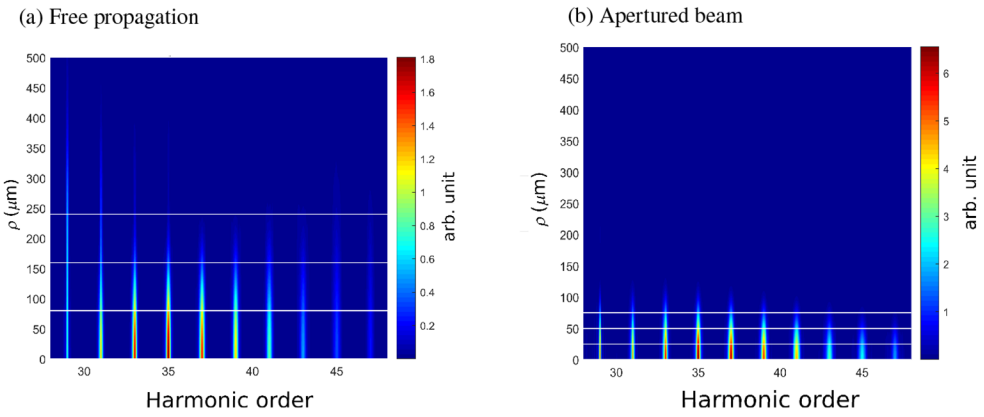

Fig. 7. Spatially resolved spectra for free propagation (a) and apertured beam (b) at 2.9 m from IR focus. White lines correspond to radii at which temporal structure are depicted in Fig. 9, and corresponds to 0, 0.5, 1.0 and 1.5 value of the critical radius. The critical radius is defined by half of the energy of the XUV energy contained inside and outside this radius as explained in the main text.

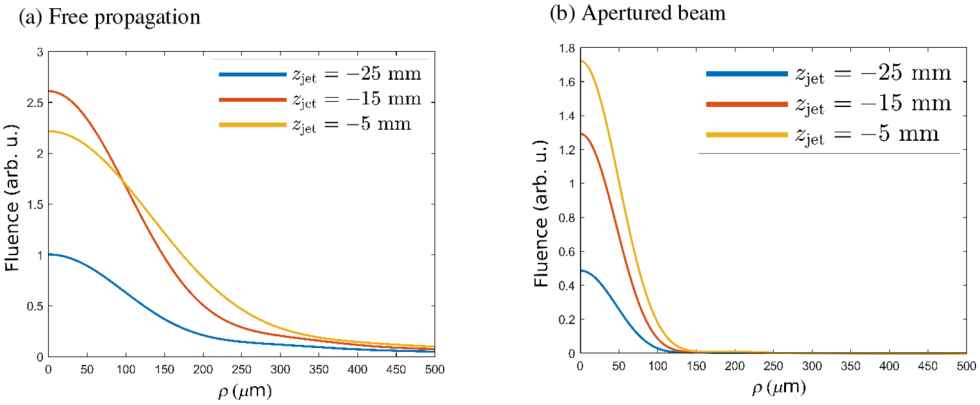

Fig. 8. Plot of the XUV fluence as a function of ρ in the far-field for $z_{jet} = -25$ mm, -15 mm and -5 mm. In (a) it is the free propagation case, in (b) it corresponds to the apertured case.

Optics EXPRESS

contained inside and outside this radius. It is defined by $\int_0^{\rho_c} \rho d\rho F(\rho) = \int_{\rho_c}^{\infty} \rho d\rho F(\rho)$ with $F(\rho)$ being the fluence presented in Fig. 8. We obtain $\rho_c = 50$ μm in the apertured case and $\rho_c = 167$ μm in the free propagation case. In Fig. 9 we plot the temporal profile of the XUV beam for different values of ρ, in the vicinity of ρ_c, for the field free propagation (a) and with filtering (b). We chose the values of the radius in the range going from 0 up to 1.5 times the critical radius. We first notice a slower drop of the intensity as ρ increases in the apertured beam. This can be explained when considering the Perceval's identity. In Fig. 7(a) we clearly see that only small fraction of the spectrum contributes when ρ increases. On the contrary in Fig. 7(b) almost all harmonics contribute equally in amplitude for all the values of ρ. This behavior can appear in contradiction with the larger fluence distribution obtained in Fig. 8(a) and it simply means that only the lower order harmonics contribute to the signal for large values of ρ leading to a pulse train having a longer pulse. This is detrimental if one considers the production of ultra-short pulses.

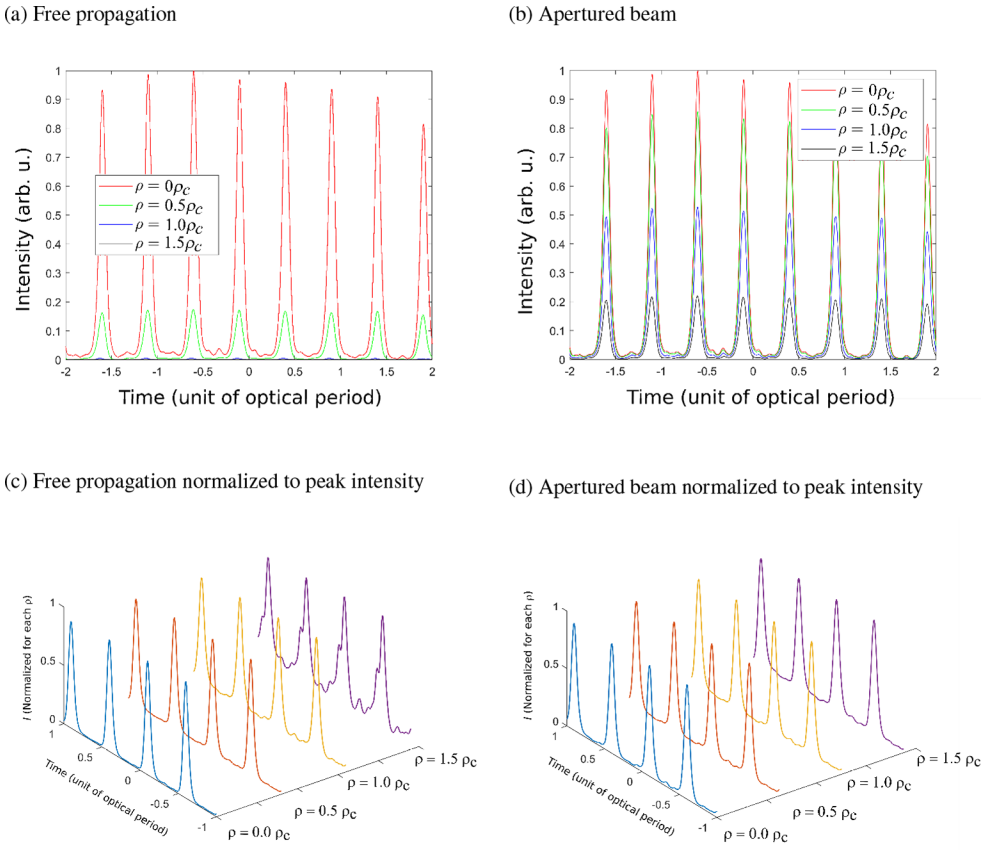

Fig. 9. The intensity temporal profiles for jet position 15 mm before IR focus at radii specified by white lines in Fig. 7. We compare the case with (b) and without (a) the pinhole but at different radii for which harmonic intensities are comparable. The values of ρ are chosen around the critical radius, defining the radius at which the energy is equally shared between the inner and outer region. $\rho_c = 50$ μm for the apertured case and $\rho_c = 167$ μm for the free case. In figs. (c) and (d), the distributions have been normalized for each value of ρ.

One can also notice that the apertured beam presents a more regular evolution of the attosecond pulse train with ρ in the apertured case. This is more apparent when we consider the Fig. 9(c) for which the peak intensity has been normalized in the free propagation case. In particular, in the

Optics EXPRESS

free propagation condition for $\rho = 1.5\rho_c$ a double hump structure appears in the temporal profile due to the contribution of the long trajectories. This temporal profile becomes even more heckled for larger radii. Consequently, the approach presented here not only allows for spatial filtering but also enables for spectral filtering (thus temporal shaping) so that a more regular XUV beam, both spatially and temporally, is obtained.

As we have investigated in the previous section, the optics-free focusing properties, although promising, does not yet allow for focusing at long distances where the IR beam would be fully rejected. Nevertheless, these far-field properties are beneficial in the context of refocusing of the XUV beam using only one reflective mirror in order to image the generated beam. In particular, in the case when the generating plane is equivalent as being a virtual source, these focii will become real points near the focusing plane of the mirror. This means that all the values of z_{jet} can be exploited in this configuration unlike for the case of real focusing for which only a given range of z_{jet} will satisfy this condition. The use of the pinhole located near XUV focus, as presented in this work, is different than using an iris in the far field as usually performed. In the second case, the iris acts as a spatial filter in the Fourier space and can, from that point of view, apodize the spatial distribution leading to similar properties as mentioned before in the case where the pinhole is located in the intermediate field (i.e. near focus). The main difference lies in the fact that filtering of frequencies can be controlled in the case where the pinhole is located in the intermediate field as it can be either in the near field for some harmonics and in the far field for others.

The conclusion drawn in this section shows the strong impact of the filtering on the spatio-spectral properties of the XUV beam when the pinhole is located in the intermediate field (in the region of real focusing). We have demonstrated this effect in the case of $z_{jet} = -15$ mm where the transmittance function is almost independent on the harmonic order. But this conclusion is general and not limited to the specific value of -15 mm as can be seen by the spatial distribution of the XUV beam as a function of ρ for different z_{jet}.

At $z_{jet} = -15$ mm, despite the fact that the frequency content of the XUV beam can be controlled going from apertured to free propagation, the effect on the temporal evolution and on the beam spatial profile are made more homogeneous ensuring reduced spatio-temporal couplings in the apertured configuration. This effect could be of strong interest for applications and is fundamentally different than filtering in the far-field as usually performed which does not ensure the XUV beam homogeneity nor strong rejection of the fundamental beam or XUV tunability.

5. Conclusion

We investigated the spatial characteristics of XUV harmonic beams as a function of the position of the generating medium relative to the IR focus. From the SWORD technique, we characterized the XUV intensity spatial profiles and wavefronts in order to retrieve both the size and position of the waists of the Gaussian XUV beam. We observed that optics-free focusing of high-order harmonics can be obtained in specific conditions. This constitutes a direct observation which confirms our previous result presented in [23] where optics-free focusing of harmonics was shown qualitatively using spatial chirp of the generating beam. While diverging harmonics are generated with virtual waists as small as 5 μm, converging XUV beams are also produced with waists of $5 - 20$ μm and can be focused down at distances of approximately $4 \times z_{R-IR}$ (120 mm) after the IR focus or $5 \times z_{R-IR}$ after the gas jet. We emphasize that no XUV optics are used in this work, thus preserving high XUV pulse energy. This approach is a way to reach high XUV intensities and should benefit to non-linear XUV-pump-XUV-probe experiments since we demonstrate that the harmonics are seldom focused at the same position.

Taking advantage of the control of the harmonic focusing, we demonstrated experimentally and theoretically tunable XUV spectral filtering without resorting to XUV optics or metallic filter. The achieved spectral filtering ensures that the harmonics have similar spatial profiles

Optics EXPRESS

after filtering. It is characterized by high XUV transmission, full tunability (low-pass, high-pass or broadband filter) controlled by adjusting the gas jet position with respect to the IR focus, while maintaining a strong rejection of the IR fundamental and low-order harmonic beams. This technique allows band-pass transmission with high spectral selectivity and contrast. It is of particular interest, for instance, in studying molecular dynamics with experiments based on photoelectron spectroscopy. We reproduced most of the experimental observations by means of the TDSE-model. First, we obtained similar evolution of the transmittance as a function of both harmonic order and jet-position and observed similar beam profile after the pinhole. Second, we confirmed the pinhole trimming ability by filtering the more divergent part of the beam leading to homogeneous properties of the spatio-temporal XUV beam. Our filtering technique improves the XUV beam quality and ensures a regular evolution of the spatio-temporal attosecond beam.

Funding. Laserlab-Europe (EU-H2020 GA N°871124); Conseil Régional Aquitaine (Contrat N°184289); Agence Nationale de la Recherche (ANR-16-CE30-0012).

Acknowledgements. We acknowledge the financial support from the Agence Nationale de la Recherche (ANR) through the 'CIRCE' project (ANR-16-CE30-0012), from the Région Nouvelle-Aquitaine through the 'OFIMAX' project (contrat N° 184289) and also Laserlab-Europe EU-H2020 GA N° 871124. Computations were performed using HPC resources from the MCIA (Mésocentre de Calcul Intensif Aquitain) of the Université de Bordeaux and of the Université de Pau et des Pays de l'Adour. Portions of the theoretical results were carried out at ELI Beamlines, a European user facility operated by the Institute of Physics of the Academy of Sciences of the Czech Republic.

Disclosures. The authors declare no conflicts of interest.

Data availability. Data underlying the results presented in this paper are not publicly available at this time but may be obtained from the authors upon reasonable request.

References

1. A. McPherson, G. Gibson, H. Jara, U. Johann, T. S. Luk, I. A. McIntyre, K. Boyer, and C. K. Rhodes, "Studies of multiphoton production of vacuum-ultraviolet radiation in the rare gases," J. Opt. Soc. Am. B **4**(4), 595–601 (1987).
2. M. Ferray, A. L'Huillier, X. F. Li, L. A. Lompre, G. Mainfray, and C. Manus, "Multiple-harmonic conversion of 1064 nm radiation in rare gases," J. Phys. B: At., Mol. Opt. Phys. **21**(3), L31–L35 (1988).
3. F. Calegari, G. Sansone, S. Stagira, C. Vozzi, and M. Nisoli, "Advances in attosecond science," J. Phys. B: At., Mol. Opt. Phys. **49**(6), 062001 (2016).
4. Z. Chang, P. B. Corkum, and S. R. Leone, "Attosecond optics and technology: progress to date and future prospects [Invited]," J. Opt. Soc. Am. B **33**(6), 1081–1097 (2016).
5. S. L. Cousin, N. Di Palo, B. Buades, S. M. Teichmann, M. Reduzzi, M. Devetta, A. Kheifets, G. Sansone, and J. Biegert, "Attosecond Streaking in the Water Window: A New Regime of Attosecond Pulse Characterization," Phys. Rev. X **7**(4), 041030 (2017).
6. F. Lépine, M. Y. Ivanov, and M. J. J. Vrakking, "Attosecond molecular dynamics: fact or fiction?" Nat. Photonics **8**(3), 195–204 (2014).
7. A. Marciniak, V. Despré, T. Barillot, A. Rouzée, M. C. E. Galbraith, J. Klei, C.-H. Yang, C. T. L. Smeenk, V. Loriot, S. N. Reddy, A. G. G. M. Tielens, S. Mahapatra, A. I. Kuleff, M. J. J. Vrakking, and F. Lépine, "XUV excitation followed by ultrafast non-adiabatic relaxation in PAH molecules as a femto-astrochemistry experiment," Nat. Commun. **6**(1), 7909–7914 (2015).
8. M. Nisoli, P. Decleva, F. Calegari, A. Palacios, and F. Martín, "Attosecond Electron Dynamics in Molecules," Chem. Rev. **117**(16), 10760–10825 (2017).
9. S. Witte, V. T. Tenner, D. W. E. Noom, and K. S. E. Eikema, "Lensless diffractive imaging with ultra-broadband table-top sources: from infrared to extreme-ultraviolet wavelengths," Light: Sci. Appl. **3**(3), e163 (2014).
10. G. K. Tadesse, R. Klas, S. Demmler, S. Hädrich, I. Wahyutama, M. Steinert, C. Spielmann, M. Zürch, T. Pertsch, A. Tünnermann, J. Limpert, and J. Rothhardt, "High speed and high resolution table-top nanoscale imaging," Opt. Lett. **41**(22), 5170–5173 (2016).
11. B. Manschwetus, L. Rading, F. Campi, S. Maclot, H. Coudert-Alteirac, J. Lahl, H. Wikmark, P. Rudawski, C. M. Heyl, B. Farkas, T. Mohamed, A. L'Huillier, and P. Johnsson, "Two-photon double ionization of neon using an intense attosecond pulse train," Phys. Rev. A **93**(6), 061402 (2016).
12. T. R. Barillot, P. Matia-Hernando, D. Greening, D. J. Walke, T. Witting, L. J. Frasinski, J. P. Marangos, and J. W. G. Tisch, "Towards XUV pump-probe experiments in the femtosecond to sub-femtosecond regime: New measurement of the helium two-photon ionization cross-section," Chem. Phys. Lett. **683**, 38–42 (2017).
13. E. Frumker, G. G. Paulus, H. Niikura, A. Naumov, D. M. Villeneuve, and P. B. Corkum, "Order-dependent structure of high harmonic wavefronts," Opt. Express **20**(13), 13870–13877 (2012).
14. C. Bourassin-Bouchet, L. Barreau, V. Gruson, J.-F. Hergott, F. Quéré, P. Salières, and T. Ruchon, "Quantifying Decoherence in Attosecond Metrology," Phys. Rev. X **10**(3), 031048 (2020).

Optics EXPRESS

15. S. Chatziathanasiou, S. Kahaly, D. Charalambidis, P. Tzallas, and E. Skantzakis, "Imaging the source of high-harmonics generated in atomic gas media," Opt. Express **27**(7), 9733–9739 (2019).
16. D. T. Lloyd, K. O'Keeffe, P. N. Anderson, and S. M. Hooker, "Gaussian-Schell analysis of the transverse spatial properties of high-harmonic beams," Sci. Rep. **6**(1), 30504–30512 (2016).
17. H. Wikmark, C. Guo, J. Vogelsang, P. W. Smorenburg, H. Coudert-Alteirac, J. Lahl, J. Peschel, P. Rudawski, H. Dacasa, S. Carlström, S. Maclot, M. B. Gaarde, P. Johnsson, C. L. Arnold, and A. L'Huillier, "Spatiotemporal coupling of attosecond pulses," Proc. Natl. Acad. Sci. **116**(11), 4779–4787 (2019).
18. I. Makos, I. Orfanos, A. Nayak, J. Peschel, B. Major, I. Liontos, E. Skantzakis, N. Papadakis, C. Kalpouzos, M. Dumergue, S. Kühn, K. Varju, P. Johnsson, A. L'Huillier, P. Tzallas, and D. Charalambidis, "A 10-gigawatt attosecond source for non-linear XUV optics and XUV-pump-XUV-probe studies," Sci. Rep. **10**(1), 3759–3776 (2020).
19. C. Bourassin-Bouchet, M. M. Mang, F. Delmotte, P. Chavel, and S. de Rossi, "How to focus an attosecond pulse," Opt. Express **21**(2), 2506–2520 (2013).
20. C. Valentin, D. Douillet, S. Kazamias, Th. Lefrou, G. Grillon, F. Augé, G. Mullot, Ph. Balcou, P. Mercère, and Ph. Zeitoun, "Imaging and quality assessment of high-harmonic focal spots," Opt. Lett. **28**(12), 1049–1051 (2003).
21. J. Chalupský, L. Juha, V. Hájková, J. Cihelka, L. VyšÍn, J. Gautier, J. Hajdu, S. P. Hau-Riege, M. Jurek, J. Krzywinski, R. A. London, E. Papalazarou, J. B. Pelka, G. Rey, S. Sebban, R. Sobierajski, N. Stojanovic, K. Tiedtke, S. Toleikis, T. Tschentscher, C. Valentin, H. Wabnitz, and P. Zeitoun, "Non-thermal desorption/ablation of molecular solids induced by ultra-short soft x-ray pulses," Opt. Express **17**(1), 208–217 (2009).
22. C. Bourassin-Bouchet, S. de Rossi, J. Wang, E. Meltchakov, A. Giglia, N. Mahne, S. Nannarone, and F. Delmotte, "Shaping of single-cycle sub-50-attosecond pulses with multilayer mirrors," New J. Phys. **14**(2), 023040 (2012).
23. L. Quintard, V. Strelkov, J. Vabek, O. Hort, A. Dubrouil, D. Descamps, F. Burgy, C. Péjot, E. Mével, F. Catoire, and E. Constant, "Optics-less focusing of XUV high-order harmonics," Sci. Adv. **5**(4), eaau7175 (2019).
24. L. Drescher, O. Kornilov, T. Witting, G. Reitsma, N. Monserud, A. Rouzée, J. Mikosch, M. J. J. Vrakking, and B. Schütte, "Extreme-ultraviolet refractive optics," Nature **564**(7734), 91–94 (2018).
25. A. Olofsson, E. R. Simpson, N. Ibrakovic, S. Bengtsson, and J. Mauritsson, "Spatial control of extreme ultraviolet light with opto-optical phase modulation," Opt. Lett. **46**(10), 2356–2359 (2021).
26. S. R. Abbing, F. Campi, F. S. Sajjadian, N. Lin, P. Smorenbur, and P. M. Kraus, "Divergence Control of High-Harmonic Generation," Phys. Rev. Appl. **13**(5), 054029 (2020).
27. E. Frumker, G. G. Paulus, H. Niikura, D. M. Villeneuve, and P. B. Corkum, "Frequency-resolved high-harmonic wavefront characterization," Opt. Lett. **34**(19), 3026–3028 (2009).
28. T. Wodzinski, S. Künzel, J. C. P. Koliyadu, M. Hussain, B. Keitel, G. O. Williams, P. Zeitoun, E. Plönjes, and M. Fajardo, "High-harmonic generation wave front dependence on a driving infrared wave front," Appl. Opt. **59**(5), 1363–1370 (2020).
29. Q. Zhang, K. Zhao, J. Li, M. Chini, Y. Cheng, Y. Wu, E. Cunningham, and Z. Chang, "Suppression of driving laser in high harmonic generation with a microchannel plate," Opt. Lett. **39**(12), 3670–3673 (2014).
30. F. Catoire, A. Ferré, O. Hort, A. Dubrouil, L. Quintard, D. Descamps, S. Petit, F. Burgy, E. Mével, Y. Mairesse, and E. Constant, "Complex structure of spatially resolved high-order-harmonic spectra," Phys. Rev. A **94**(6), 063401 (2016).
31. The thin medium approximation can be used when i- the size of the generating medium is small as compared to the evolution of the ir intensity profile ii- the phase matching condition do not change during the propagation iii- the propagation does not affect the ir temporal profile. this is case when the rayleigh length of the laser is larger than the gas jet thickness for instance.
32. M. Lewenstein, Ph. Balcou, M. Yu. Ivano, A. L'Huillier, and P. B. Corkum, "Theory of high-harmonic generation by low-frequency laser fields," Phys. Rev. A **49**(3), 2117–2132 (1994).
33. M. B. Gaarde, F. Salin, E. Constant, Ph. Balcou, K. J. Schafer, K. C. Kulander, and A. L'Huillier, "Spatiotemporal separation of high harmonic radiation into two quantum path components," Phys. Rev. A **59**(2), 1367–1373 (1999).
34. M. B. Gaarde and K. J. Schafer, "Quantum path distributions for high-order harmonics in rare gas atoms," Phys. Rev. A **65**(3), 031406 (2002).
35. L. Rego, J. S. Román, A. Picón, L. Plaja, and C. Hernández-García, "Nonperturbative Twist in the Generation of Extreme-Ultraviolet Vortex Beams," Phys. Rev. Lett. **117**(16), 163202 (2016).
36. S. Carlström, J. Preclíková, E. Lorek, E. W. Larsen, C. M. Heyl, D. Paleček, D. Zigmantas, K. J. Schafer, M. B. Gaarde, and J. Mauritsson, "Spatially and spectrally resolved quantum path interference with chirped driving pulses," New J. Phys. **18**(12), 123032 (2016).
37. M. B. Gaarde, J. Tate, and K. J. Schafer, "Macroscopic aspects of attosecond pulse generation," J. Phys. B: At., Mol. Opt. Phys. **41**(13), 132001 (2008).